This article has been accepted for publication in IEEE Transactions on Antennas and Propagation. This is the author's version which has not been fully edited and content may change prior to final publication. Citation information: DOI 10.1109/TAP.2025.3590571



# Broadband Holographic Mode Synthesis Between Adjacent Resonances for a Low-Profile Thin-Microstrip Antenna-Fed Metasurface

Byeongjin Kim, *Graduate Student Member, IEEE*, Seungwoo Bang, *Graduate Student Member, IEEE*, Sumin Yun, Hosaeng Kim, *Member, IEEE*, and Jungsuek Oh, *Senior Member, IEEE*

***Abstract*—This paper proposes a novel technique for designing a broadside-radiating, low-profile grounded-dipole antenna—referred to here as a low-profile thin-microstrip antenna—that achieves wide bandwidth by using characteristic mode analysis and a holographic metasurface. Initially, a 3×3 subwavelength patch array is stacked on a grounded dipole antenna to achieve wideband impedance matching. There are two resonant frequencies: one corresponding to the thin-microstrip and the other to the patch array. To separate these resonant frequencies, a thin-microstrip-oriented slot is implemented in the center patch of the array. The deteriorated impedance matching at the center of the bandwidth (14 GHz) caused by the center-patch-slot is addressed by integrating a holographic metasurface around the patch array, which introduces an additional surface-wave propagating mode. The simulated and measured -10 dB impedance bandwidths are 25.5% and 24.9%, respectively, with an ultra-thin profile of 0.025$\lambda_0$ at the center frequency.**

***Index Terms*—dipole antenna, ultra-thin, wideband, holographic metasurface, 6G upper-mid band**

## I. Introduction

DIPOLE antennas are widely employed in wireless-communication systems because of their inherently broad bandwidth. To allow surface mounting on the outermost shell of compact devices, grounded dipole antennas that radiate in the broadside direction have been investigated [1]– [8]. As operating frequencies increase with the advent of 5G and 6G services, consumer products such as smartphones are becoming progressively thinner, intensifying the demand for low-profile antennas [9]– [13]. When a grounded dipole is sufficiently thinned, its electromagnetic behavior converges toward that of a microstrip patch. For clarity, we therefore refer to such a low-profile grounded dipole as a thin microstrip antenna, distinct from a conventional patch antenna. Wideband thin-microstrip antennas have been realized by incorporating high-impedance surfaces (HISs) [3], artificial magnetic conductors (AMCs) [4], [5], or parasitic elements [6], [7].

Meanwhile, a novel category of metasurface antennas (metantennas) with wideband characteristics has been studied [14]- [19]. The subwavelength-sized patch elements are stacked over various types of feed antennas [14]- [17], to introduce multi-resonance for wideband operation. A few studies have reported metantennas with thin-microstrip feed antennas [18]- [19]. In [18], a uniform-sized subwavelength patch array was placed very closely below the thin-microstrip antenna with a distance of 0.0038$\lambda$, to introduce the propagation of TM and TE surface wave modes for wideband performance. In [19], a uniform-sized subwavelength patch array was stacked very closely over the thin-microstrip antenna, with a distance of 30 $\mu$m, equivalent to 0.0032$\lambda_0$ at the center frequency, to introduce multi-resonance through strong electromagnetic coupling between the thin-microstrip antenna and the patch array. However, placing a metasurface very close to the thin-microstrip antenna is so challenging that it requires sophisticated fabrication, especially for high-frequency bands like 5G and 6G.

The holographic metasurface antenna (HMA) is a traveling-wave antenna that transforms surface waves propagating over the aperture into radiating waves by employing non-uniform-sized subwavelength elements with modulated surface reactance [20]- [21]. The HMA is composed of a surface wave launcher, which excites surface waves over the wide aperture, and subwavelength elements comprising the holographic metasurface (HM). One of the commonly used HM elements is the square patch.

In this paper, a novel approach for the bandwidth enhancement of a low-profile thin-microstrip antenna is proposed. First, a 3×3 subwavelength patch array is stacked over the thin-microstrip antenna for multi-resonance. Second, a slot is implemented in the center patch of the array to separate the two resonant frequencies. It is concluded from the characteristic mode analysis (CMA) that there are two resonant frequencies, corresponding to the thin-microstrip antenna and the patch array, respectively. Finally, the deteriorated impedance matching between the two resonant frequencies is addressed by integrating a holographic metasurface around the patch array, which introduces a surface-wave propagating mode. As a result, the ultrathin wideband antenna is designed to cover two frequency bands: 12.7-13.25 GHz and 14.8-15.3 GHz, which are candidates for the upcoming 6G upper-mid frequency bands.

## II. Antenna Configuration

Fig. 1 shows the entire configuration of the proposed antenna. Two 254 $\mu$m thick Rogers RT/duriod 6010LM dielectric substrates, with $\epsilon_r = 10.2$ and $\tan\delta = 0.0023$, are bonded using a 38 $\mu$m thick Rogers 2929 bonding layer with $\epsilon_r = 2.94$ and $\tan\delta = 0.004$. Such high-permittivity substrates were chosen to shorten the guided wavelength, thereby reducing the overall antenna dimensions. A horizontally oriented dipole antenna is printed on the lower dielectric substrate, with one arm connected to the bottom ground via a via and the other arm connected to one end of the coplanar waveguide (CPW) line implemented in the bottom ground. The metasurface, composed of square patches with a unit cell period of 3 mm in both the x- and y-axis directions, is stacked on top of the upper dielectric substrate. Notably, a thin-microstrip-oriented slot is implemented in the center patch of the metasurface. The CPW line and the antenna substrates are extended in the y-axis direction for connector integration in measurements. The aperture area of the antenna is 40 mm×40 mm,

Manuscript created Aug., 2024.

This work was supported in part by Samsung Electronics Co., Ltd., and in part by an Institute of Information and Communications Technology Planning and Evaluation (IITP) through the Korean Government [Ministry of Science and ICT (MSIT)], "Innovative Fusion Technologies of Intelligent Antenna Material/Structure/Network for THz 6G," under Grant 2021-0-00763. (Corresponding author: Jungsuek Oh.).

Byeongjin Kim, Seungwoo Bang, and Jungsuek Oh are affiliated with the Institute of New Media and Communications (INMC), Department of Electrical and Computer Engineering, Seoul National University, Seoul 08826, South Korea (e-mail: jungsuek@snu.ac.kr).

Sumin Yun and Hosaeng Kim are with Samsung Electronics Co., Ltd., Suwon, South Korea.

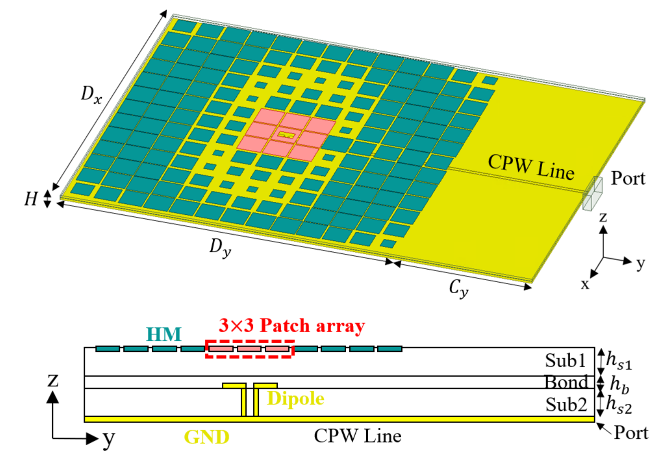


Fig. 1. Configuration of the proposed ultra-thin wideband antenna, highlighting its key design features. $D_x = D_y$ =40 mm, $H$ =0.546 mm, $C_y$ =15 mm, $h_{s1} = h_{s2}$ =0.254 mm, and $h_b$ =0.038 mm.

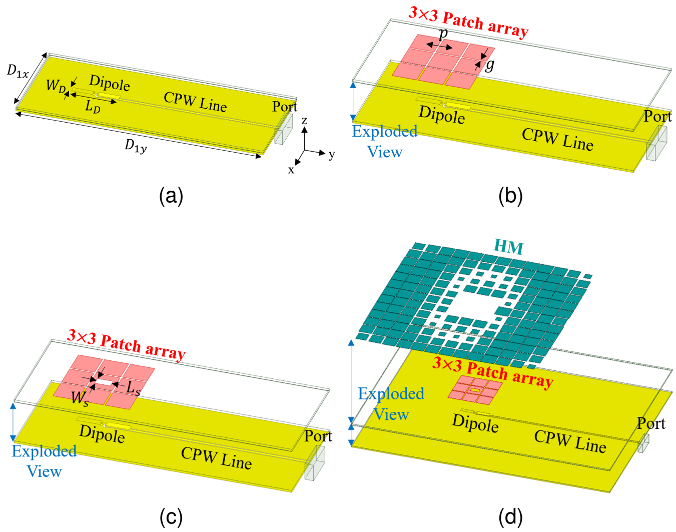


Fig. 2. Evolution of the proposed antenna: (a) Ant. I: A low-profile grounded dipole (thin-microstrip) antenna; (b) Ant. II: A 3×3 patch array stacked on Ant. I; (c) Ant. III: A slot implemented in the center patch of Ant. II; and (d) Ant. IV: A holographic metasurface integrated around Ant. III. $D_{1x}$ =13 mm, $D_{1y}$ =17 mm, $W_D$ =0.75 mm, $L_D$ =6.1 mm, $p$ =3 mm, $g$ =0.2 mm, $L_s$ =1.8 mm, and $W_s$ =1 mm.

or $1.87\lambda_0 \times 1.87\lambda_0$, where $\lambda_0$ refers to the free-space wavelength at 14 GHz. The total thickness of the antenna is $0.025\lambda_0$.

Fig. 2 shows the evolution of the proposed antenna. Ant. I is a low-profile thin-microstrip antenna, which is not yet impedance matched. The length and width of the thin-microstrip are 6.1 mm and 0.75 mm, respectively. A 3×3 subwavelength patch array with a uniform patch size of 2.8 mm×2.8 mm and 0.2 mm gaps between patches is stacked on Ant. I, referred to as Ant. II. The center-to-center distance between these patches 3 mm. A thin-microstrip-oriented slot is then implemented in the center patch of Ant. II, creating Ant. III. Finally, Ant. IV incorporates a holographic metasurface (HM) around Ant. III. The HM consists of $13 \times 13 - 3 \times 3 = 160$ non-uniformly sized square patches with a constant center-to-center distance of 3 mm.

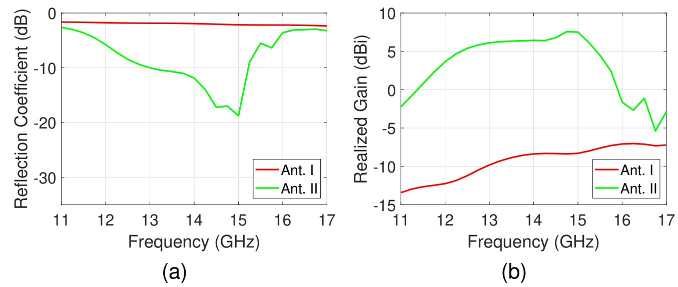


Fig. 3. (a) Simulated reflection coefficients and (b) realized gain of Ant. I and Ant. II.

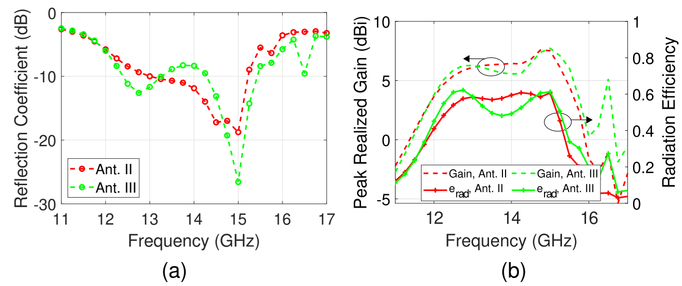


Fig. 4. (a) Simulated reflection coefficients and (b) realized gain and radiation efficiency of Ant. II and Ant. III.

## III. Low-Profile Thin-Microstrip With Patch Array

### A. *Integration of 3×3 Patch Array*

The initial impedance matching of the thin-microstrip antenna is achieved with a 3×3 patch array stacked on the thin-microstrip antenna, as shown in Fig. 3. Ant. II exhibits a decent -10 dB impedance bandwidth of 15.8%, ranging from 13.0 GHz to 15.2 GHz. The chosen design parameters, $p$ = 3 mm and $g$ = 0.2 mm, are optimal for covering 12.7-13.25 GHz and 14.8-15.3 GHz, which are two candidates for the upcoming 6G upper-mid frequency bands.

### B. *Ant. II to Ant. III: Implementation of a Slot in The Center Patch*

To further increase the bandwidth of Ant. II, a thin-microstrip-oriented slot is implemented in the center patch of the array, creating Ant. III. Even if only the center patch is slotted, that slot's proximity to the underlying thin-microstrip provides sufficient control over the electromagnetic coupling between the patch and the thin-microstrip, and thus over the antenna's impedance matching. Fig. 4(a) shows that adopting this slot separates the two resonant frequencies of the antenna. However, the impedance matching of the antenna at the midpoint between the two resonant frequencies, including 14 GHz, is deteriorated, which will be addressed by integrating a holographic mode in Section IV. Therefore, the total -10 dB impedance bandwidth of Ant. III is 14.4% (from 12.4 GHz to 13.3 GHz and from 14.3 GHz to 15.4 GHz), which is similar to that of Ant. II. The realized gain and radiation efficiency are also reduced at the center frequency because of the poor impedance matching, as shown in Fig. 4(b). Considering moderate separation of the two resonant frequencies and moderate deterioration of impedance matching at those frequencies, $W_s$ and $L_s$ were determined to be 1 mm and 1.8 mm, respectively.

### C. *Characteristic Mode Analysis on Ant. II and Ant. III*

To identify the resonant modes contributing to the radiation of Ant. II and Ant. III, characteristic mode analysis (CMA) was performed

This article has been accepted for publication in IEEE Transactions on Antennas and Propagation. This is the author's version which has not been fully edited and content may change prior to final publication. Citation information: DOI 10.1109/TAP.2025.3590571



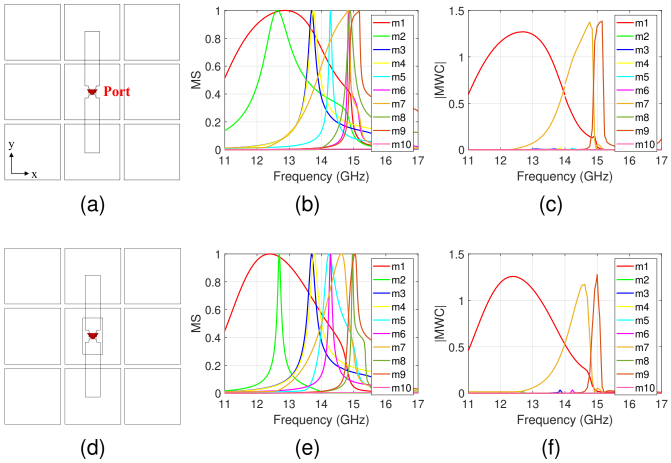


Fig. 5. Geometric modeling for the characteristic mode analysis: (a) Ant. II and (d) Ant. III; modal significance (MS) for (b) the former and (e) the latter; and modal weighting coefficient (MWC) for (c) the former and (f) the latter.

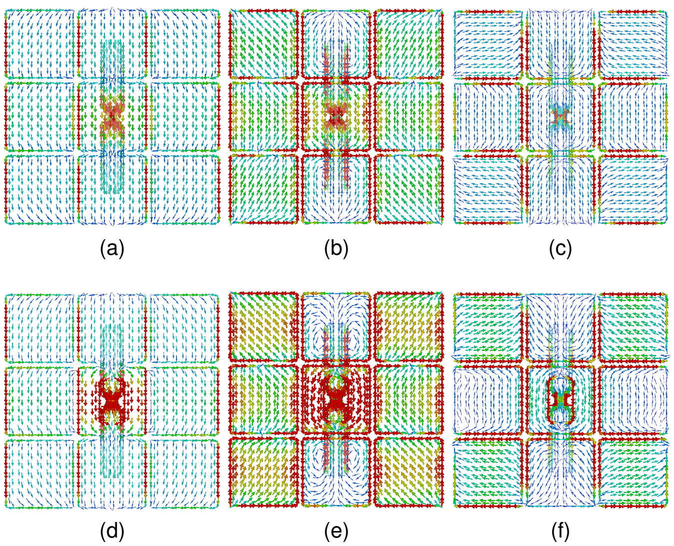


Fig. 6. Y-polarized radiating modal currents on Ant. II: (a) mode 1 at 12.5 GHz, (b) mode 7 at 14.5 GHz, and (c) mode 9 at 15 GHz; and on Ant. III: (d) mode 1 at 12.5 GHz, (e) mode 7 at 14.5 GHz, and (f) mode 9 at 15 GHz. Plots (c) and (f) are shown with a 0–500 A/m range, while the others are shown with a 0–100 A/m range.

using the CST Multilayer Solver [14]. Fig. 5 shows the geometric models, modal significance (MS), and modal weighting coefficients (MWC) for the first ten characteristic modes above 11 GHz for both antennas, assuming an infinite bottom ground plane. Among these modes, only three—modes 1, 7, and 9—are strongly excited and contribute significantly to radiation, as indicated by the MWC plots, while the remaining modes remain suppressed. Fig. 6 shows the modal current distributions for these resonant modes on Ant. II and Ant. III at their respective resonant frequencies. Mode 1 radiates near 12.5 GHz with y-polarization and is primarily excited by the thin-microstrip. Its current distribution resembles that of a typical half-wavelength dipole, with minimal coupling to the $3 \times 3$ patch array. Mode 7, radiating near 14.5 GHz, is one of the resonant modes of the $3 \times 3$ patch array and also exhibits y-polarization. Mode 9 radiates with mixed polarizations; however, y-polarization is dominant in Ant. III, as y-polarized currents are concentrated on the center patch of the $3 \times 3$ array, particularly around the slot.

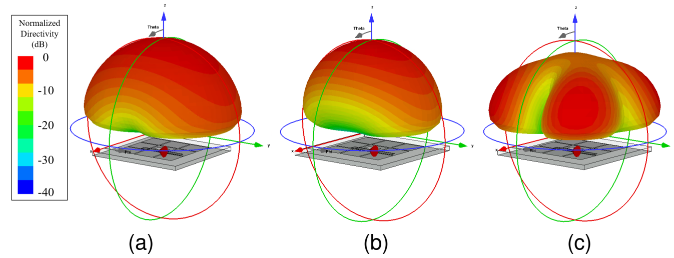


Fig. 7. The modal radiation patterns of Ant. III for (a) mode 1 at 12.5 GHz, (b) mode 7 at 14.5 GHz, and (c) mode 9 at 15 GHz.

The modal radiation patterns of modes 1 and 7, shown in Fig. 7, exhibit the desired broadside radiation characteristics. Mode 9 radiates with y-polarization in the broadside direction and with x-polarization in the endfire directions. As shown in Fig. 4(a), mode 9 actually radiates at a shifted frequency of 15.75 GHz due to discrepancies between the simplified CMA model and the HFSS-simulated model. Similar frequency shifts are observed for mode 1 (to 12.75 GHz) and mode 7 (to 15.0 GHz). Notably, the shifted frequency of mode 9 lies outside the operational band of Ant. III. Therefore, broadside radiation and a wide impedance bandwidth—from 12.0 GHz to 15.5 GHz—can be simultaneously achieved. These modes, along with the holographic mode employed in Ant. IV, will be revisited in Section V.

## IV. Holographic Metasurface for Impedance Matching at Center Frequency

### A. Holography Principle

The concept of optical holography has been implemented in the design of traveling antennas [20], [21]. A holographic metasurface antenna (HMA) consists of a surface wave launcher (SWL) and a holographic metasurface (HM). The SWL excites surface wave propagation over the HM. The HM, composed of non-uniform subwavelength elements, then transforms the surface wave into the desired radiating wave. Here, the surface wave initially excited over the aperture is referred to as the reference wave ($\psi_{ref}$), while the required surface wave to be distributed over the aperture to generate the desired radiating wave is referred to as the object wave ($\psi_{obj}$). The surface impedance of each HM element is modulated by changing its design parameters to transform $\psi_{ref}$ into $\psi_{obj}$ over the aperture, with their impedance assigned as follows:

$$Z_s = 1j \times [X + M \times \Re(\psi_{ref}^{*}\psi_{obj})], \quad (1)$$

where $X$ is the average surface reactance obtained for the chosen HM element type by varying its physical parameters, and $M$ is the difference between the maximum available surface reactance and $X$.

Assuming sinusoidal waves with uniform amplitude, that is, $\psi_{ref} = \exp(j\phi_{ref})$ and $\psi_{obj} = \exp(j\phi_{obj})$, equation (1) can be rewritten as follows:

$$Z_s = 1j \times [X + M \times \cos(-\phi_{ref} + \phi_{obj})], \quad (2)$$

where $\phi_{ref}$ and $\phi_{obj}$ are the phase distributions on the aperture for the reference and object waves, respectively.

### B. Selected HM Unit Cell and Its Surface Impedance Range

Fig. 8 shows the selected square patch-type HM element, which is commonly used for its effectiveness in TM mode surface wave modulation. The simulation setup for the HM unit cell using the HFSS eigenmode solver is also shown in the figure. By assigning a

This article has been accepted for publication in IEEE Transactions on Antennas and Propagation. This is the author's version which has not been fully edited and content may change prior to final publication. Citation information: DOI 10.1109/TAP.2025.3590571



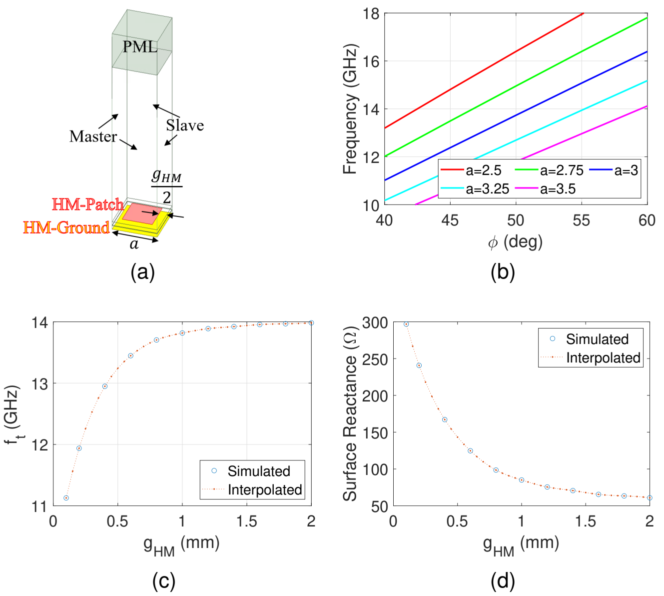


Fig. 8. (a) The square-patch type HM unit cell and its simulation setup. (b) The dispersion diagram for the HM unit cell without the patch, varying unit cell size $a$ (unit: mm). (c) The TM mode frequency $f_t$ for the HM unit cell with the patch, $a = 3$ mm, $\phi = 51°$, and varying $g_{HM}$ (unit: mm). (d) The calculated surface reactance with varying $g_{HM}$.

phase difference, $\phi$, in the x-axis direction, a dispersion diagram for the HM unit cell without a patch is first drawn, as shown in Fig. 8(b). To facilitate the integration of the HM with Ant. III, the unit cell size, $a$, is chosen to be 3 mm, which yields $\phi = 51°$ at 14 GHz. This unit cell is smaller, in terms of wavelength, than the one used in [20]. Next, as shown in Fig. 8(c), the TM mode frequency $f_t$ of the HM unit cell was obtained by sweeping the design parameter $g_{HM}$, confirming that $f_t$ and $\omega_t = 2\pi f_t$ depend on $g_{HM}$. Finally, the surface impedance, $Z_s$, of the HM unit cell is calculated as a function of $g_{HM}$ as follows:

$$Z_s = Z_0\sqrt{1 - (\phi c / a\omega_t)^2}, \tag{3}$$

as shown in Fig. 8(d), where $Z_0$ is the free-space wave impedance of 377Ω. The surface reactance $X_s$ is calculated to range from 61Ω to 297Ω, resulting in $X = 179\Omega$ and $M = 118\Omega$.

### C. Design and Integration of Holographic Metasurface

The reference wave $\psi_{ref}$ excited on the grounded substrate aperture around Ant. III is exported from the HFSS simulation at the center positions of each HM square patch. The $\psi_{ref}$ phase distribution ($\phi_{ref}$) and the corresponding $g_{HM}$ distribution, calculated from equations (1)-(3) on the 40 mm×40 mm aperture, are shown in Fig. 9. Notably, a uniform phase distribution is assumed for $\psi_{obj}$ for broadside radiation. It is evident from Fig. 10(a) that impedance matching at 14 GHz is indeed improved by integrating the HM around Ant. III. This bandwidth is similar to the theoretical maximum bandwidth from 12 GHz to 15.5 GHz predicted by the CMA in subsection III-A. The -10 dB impedance bandwidth of Ant. IV is now widened to 25.5%, ranging from 12.19 GHz to 15.76 GHz, which is much wider than the bandwidths of Ant. I, II, and III. Fig. 10(b) shows that the antenna gain also increased around 14 GHz due to the additional surface wave propagation mode introduced by the HM integration, which contributed to antenna radiation. Specifically, the antenna gain increased by 3.07 dB, from 5.56 dBi to 8.63 dBi, at

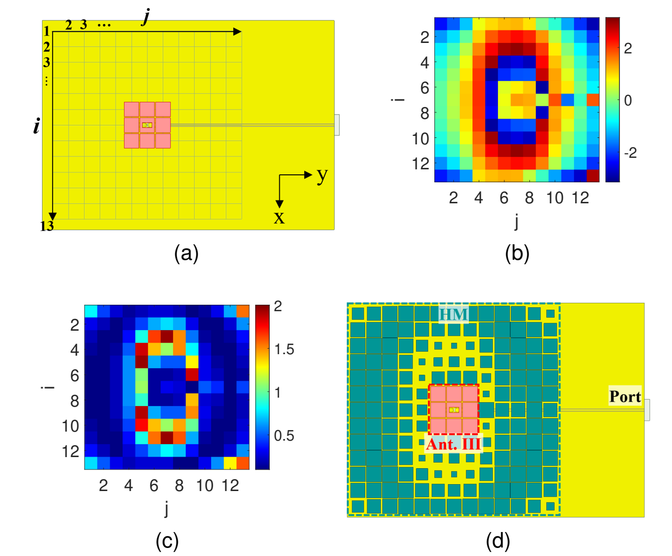


Fig. 9. (a) The 40 mm×40 mm aperture including Ant. III, and (b) the exported $\psi_{ref}$ phase distribution ($\phi_{ref}$) on the aperture. (c) The $g_{HM}$ distribution calculated on the aperture, and (d) the final Ant. IV design including HM.

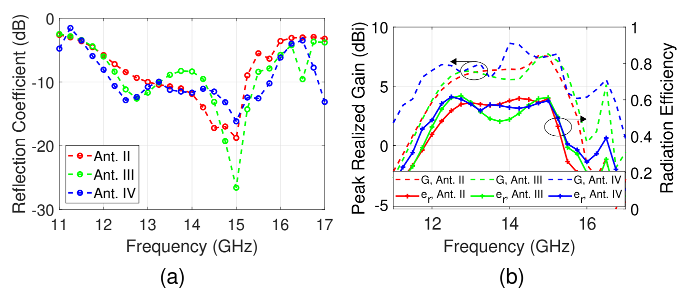


Fig. 10. (a) Simulated reflection coefficients and (b) realized gain and radiation efficiency of Ant. II, Ant. III, and Ant. IV.

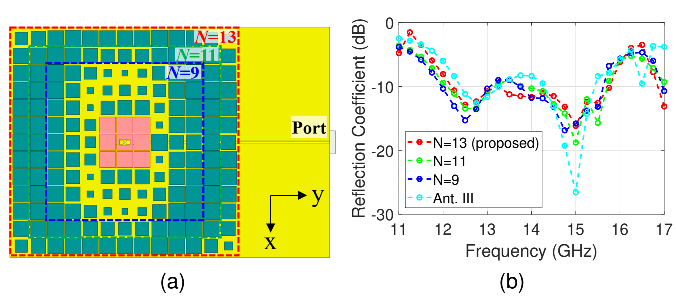


Fig. 11. The Ant. IV simulation with varying HM size of $N \times N - 3 \times 3$ (where N=9, 11, 13 (proposed)): (a) Illustration of HM modeling with varying $N$ and (b) simulated reflection coefficients.

14 GHz. It is also observed that radiation efficiency around 14 GHz increased as impedance matching improved, increasing by 6.6% at 14 GHz and 8.7% at maximum. Notably, the radiation efficiency of Ant. IV exceeds 50%, which is the criterion required for practical antennas to meet [22], across most of the bandwidth (from 12.02 GHz to 15.25 GHz).

Fig. 11 shows the influence of HM size on the bandwidth of Ant. IV. The HM size is varied by changing $N$, where the HM is composed of $N \times N$ unit cells, excluding the 3×3 patch array at the center. The results indicate that impedance matching at the

This article has been accepted for publication in IEEE Transactions on Antennas and Propagation. This is the author's version which has not been fully edited and content may change prior to final publication. Citation information: DOI 10.1109/TAP.2025.3590571



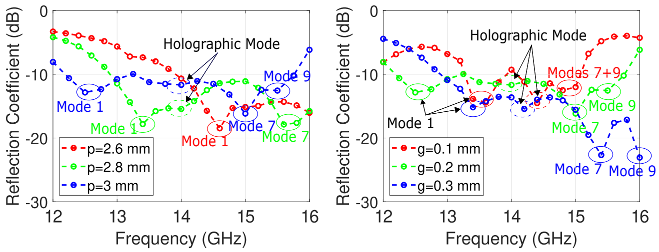


(a) (b)

Fig. 12. Simulated reflection coefficient results for Ant. IV with varying 3×3 patch array: (a) period $p$ and (b) gap $g$ (refer to Fig. 2(b)).

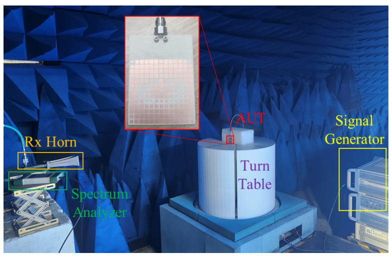


Fig. 13. Photographs of the measurement setup and the fabricated sample.

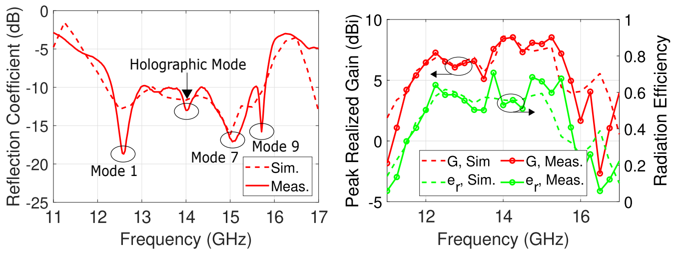


(a) (b)

Fig. 14. The simulated and measured (a) reflection coefficients and (b) realized gain and radiation efficiency of Ant. IV.

two resonant frequencies, corresponding to the thin-microstrip and the 3×3 patch array resonance, is maintained regardless of HM size, while impedance matching at 14 GHz improves. The HM size $N = 13$ is chosen to achieve a wide and continuous bandwidth across the band without losing impedance matching level.

Fig. 12 shows the simulated reflection coefficient results from the parametric studies on the 3×3 patch array period $p$ and gap $g$ noted in Fig. 2(b). It can be observed that the holographic mode frequency remains around 14 GHz regardless of the 3×3 patch array period and gap, while the radiating frequencies of mode 1 and mode 7 vary significantly as $p$ and $g$ change.

## V. Fabrication and Measurement

### A. Measurement Results

Fig. 13 shows the fabricated Ant. IV sample and its measurement setup. The end-launch connector is integrated into the edge of the sample where CPW line is extended. Fig. 14 shows that the simulated and measured reflection coefficients, gain, and radiation efficiency are in good agreement. The simulated and measured -10 dB impedance bandwidths are 25.5% and 24.9%, respectively, ranging from 12.19 GHz to 15.76 GHz and from 12.32 GHz to 15.80 GHz. Notably, Fig. 14(a) shows that the three resonant modes of Ant. III—mode 1 at 12.6 GHz, mode 7 at 15.1 GHz, and mode 9 at 15.7 GHz—as well as the holographic mode at 14.0 GHz, are successfully synthesized as intended. The simulated and measured peak gains are 8.6 dBi and 8.5 dBi at 14.0 GHz and 14.25 GHz, respectively. Notably, the measured radiation efficiency exceeds 50% across most of the bandwidth (from 11.97 GHz to 15.67 GHz), with peak simulated and measured radiation efficiencies of 61.6% and 70.0%. The radiation efficiency appears to exhibit higher error, which is due to the fact that a 1 dB error in measured gain can lead to a radiation efficiency error greater than 10%.

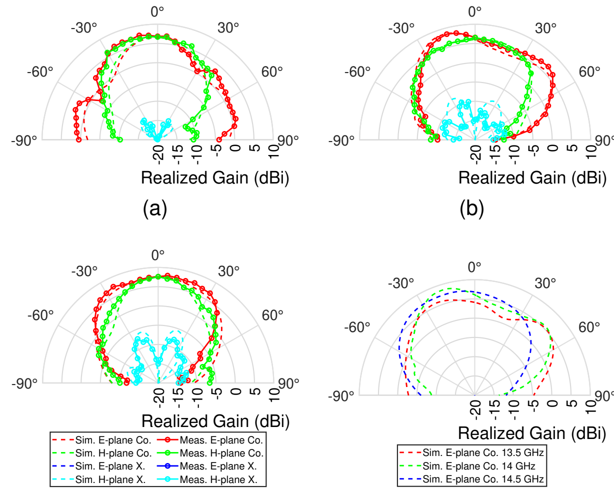


(a) (b) (c) (d)

Fig. 15. (a)–(c) Simulated and measured E- and H-plane radiation patterns of Ant. IV at 13 GHz, 14 GHz, and 15 GHz, respectively. (d) Simulated E-plane patterns at 13.5, 14, and 14.5 GHz.

Fig. 15 shows the simulated and measured E- and H-plane radiation patterns of Ant. IV at 13, 14, and 15 GHz. They are in good agreement as well. The peak gain of 8.5 dBi at 14 GHz occurs at the main beam in the direction of $(\theta, \phi) = (15^\circ, 270^\circ)$. Although the HM was designed assuming a uniform $\phi_{obj}$, which theoretically represents ideal broadside radiation ($(\theta, \phi) = (0^\circ, 0^\circ)$) with infinite gain, the small HM size and ultra-thin antenna profile restrict surface wave control by the HM and the maximum achievable gain. Nevertheless, the integration of the HM successfully contributed to the improvement of gain at the design frequency by focusing the main beam closer to the broadside radiation direction. Notably, the cross polarization discrimination (XPD) level is very good in both the E- and H-plane, being higher than 25 dB and 15 dB, respectively. Fig. 15(d) presents the E-plane radiation patterns at frequencies around the holographic mode, specifically at 13.5, 14, and 14.5 GHz. The main beams at these frequencies are directed along the $(\theta, \phi)$ direction of $(20^\circ, 270^\circ)$, $(15^\circ, 270^\circ)$, and $(14^\circ, 270^\circ)$, respectively. Although the proposed antenna radiates via a leaky mode at these frequencies, frequency scanning is relatively small because holographic mode radiation is dominant only over a narrow bandwidth. Outside this bandwidth, adjacent resonant modes 1 and 7 take over, thereby maintaining broadside radiation.

### B. Comparison With Other Low-Profile Thin-Microstrip Antennas

Table I shows a comparison of state-of-the-art low-profile wide-band thin-microstrip antennas, including the proposed Ant. IV. Because there is a tendency for the -10 dB impedance bandwidth to decrease as the antenna profile decreases, the figure-of-merit (FOM) from [23] is used for a comprehensive evaluation of profile and bandwidth. Specifically, the FOM represents the relative bandwidth that an antenna can achieve per $0.01\lambda_0$ of the antenna profile,

TABLE I
COMPARISON OF LOW-PROFILE WIDEBAND THIN-MICROSTRIP ANTENNAS WITH BROADSIDE RADIATION

| Ref. | Center Frequency (GHz) | Profile (*$\lambda_0$) | Impedance Bandwidth (%) | **BW / Profile (%) | Peak Gain (dBi) |
|---|---|---|---|---|---|
| [4] | 2.27 | 0.148 | 52.9 | 3.6 | 8.1 |
| [5] | 6 | 0.12 | 40 | 3.3 | 9.9 |
| [6] | 0.95 | 0.067 | 57.6 | 8.6 | ***4.6 |
| [7] | 2.63 | 0.22 | 110 | 5.0 | 10.5 |
| [8] | 1.5 | 0.0026 | 1.32 | 5.1 | 5.4 |
| [18] | 5 | 0.07 | 33.6 | 4.8 | 11.5 |
| [19] | 32 | 0.081 | 50 | 6.2 | 10.8 |
| This work | 14 | 0.025 | 24.9 | **9.8** | 8.5 |

* Free-space wavelength at the center frequency.
** Figure-of-merit, defined as the relative bandwidth that the antenna can achieve per $0.01\lambda_0$ of the antenna profile at the center frequency [23].
*** Assumed from the gain plot.

where $\lambda_0$ is the free-space wavelength at the center frequency. It is calculated as follows:

$$FOM = \frac{BW\ (\%)}{Profile\ (\lambda_0)/0.01}. \quad (4)$$

The proposed antenna exhibits the best FOM value of 9.8 with a moderate peak gain of 8.5 dBi. Moreover, it is designed with the lowest profile of $0.025\lambda_0$ or 0.546 mm, except for the antenna in [8], which has a narrow bandwidth. This makes it suitable for integration with many ultra-thin wireless devices and systems that operate in 6G upper-mid frequency bands.

By combining CMA with a holographic metasurface, our approach achieves an ultra-thin profile with a higher FOM than AMC-based designs [4], [5], frequency-selective-surface (FSS)-like metasurface-based designs [18], [19], or parasitic patch-based designs [7], [8]. Additionally, it provides precise mode management and enhanced tuning flexibility through a programmable HM layer. While parasitic elements require precise spacing and may introduce unwanted coupling or shift resonances, the HM layer preserves the original resonances while adding the targeted holographic mode. Through careful optimization, we have achieved a compact, manufacturable design that enhances bandwidth and gain without additional complexity.

## VI. CONCLUSION

A low-profile wideband thin-microstrip antenna with broadside radiation is proposed based on characteristic mode analysis (CMA) and the integration of a holographic metasurface (HM). A 3×3 subwavelength patch array was initially stacked on the horizontally oriented thin-microstrip antenna for impedance matching with an ultra-thin profile. The CMA revealed two resonant frequencies corresponding to the thin-microstrip and patch array resonances, respectively. Then, a thin-microstrip-oriented slot was implemented to separate the resonant frequencies and achieve a wider bandwidth. The deteriorated impedance matching between the two resonant frequencies, around 14 GHz, was improved by integrating HM around the patch array. The HM, designed for 14 GHz, enhanced impedance matching by introducing a surface wave propagating mode, which also contributed to the broadside radiation of the antenna. This bandwidth-enhancing technique, based on CMA and HMs, has significant potential for application in other types of antennas to simultaneously achieve an ultra-thin profile and wideband performance.

## ACKNOWLEDGMENT

This work was supported by Samsung Electronics, MX division.

## REFERENCES


[1] G. Cappelletti *et al.*, "A Low-Profile Printed Drop-Shaped Dipole Antenna for Wide-Band Wireless Applications," *IEEE Trans. Antennas Propag.*, vol. 59, no. 10, pp. 3526-3535, Oct. 2011.

[2] F. Gao *et al.*, "Low-Profile Dipole Antenna With Enhanced Impedance and Gain Performance for Wideband Wireless Applications," *IEEE Antennas Wireless Propag. Lett.*, vol. 12, pp. 372-375, Mar. 2013.

[3] A. Vallecchi, J. R. De Luis, F. Capolino and F. De Flaviis, "Low Profile Fully Planar Folded Dipole Antenna on a High Impedance Surface," *IEEE Trans. Antennas Propag.*, vol. 60, no. 1, pp. 51-62, Jan. 2012.

[4] M. Li, Q. L. Li, B. Wang, C. F. Zhou and S. W. Cheung, "A Low-Profile Dual-Polarized Dipole Antenna Using Wideband AMC Reflector," *IEEE Trans. Antennas Propag.*, vol. 66, no. 5, pp. 2610-2615, May 2018.

[5] Z. Jiang *et al.*, "A Low-Profile Ultrawideband Slotted Dipole Antenna Based on Artificial Magnetic Conductor," *IEEE Antennas Wireless Propag. Lett.*, vol. 21, no. 4, pp. 671-675, Apr. 2022.

[6] W. -J. Yang *et al.*, "A Compact Broadband Circularly Polarized Crossed-Dipole Antenna With a Very Low Profile," *IEEE Antennas Wireless Propag. Lett.*, vol. 18, no. 10, pp. 2130-2134, Oct. 2019.

[7] A. Verma, M. Arrawatia and G. Kumar, "Low-Profile Wideband High-Gain Folded Dipole Antenna," *IEEE Antennas Wireless Propag. Lett.*, vol. 20, no. 6, pp. 1058-1062, Jun. 2021.

[8] Z. Wu *et al.*, "Ultralow-Profile, Electrically Small, Pattern-Reconfigurable Metamaterial-Inspired Huygens Dipole Antenna," *IEEE Trans. Antennas Propag.*, vol. 68, no. 3, pp. 1238-1248, Mar. 2020.

[9] B. Kim *et al.*, "Heterogeneous Metasurface Empowering Proximate High-Permittivity Ceramic Cover for a 5G Dual-Band Millimeter-Wave Smartphone," *IEEE Trans. Antennas Propag.*, vol. 72, no. 5, pp. 4086-4094, May 2024.

[10] B. Kim and J. Oh, "Single-Glass-Layer Optically Transparent Transmitarray With High Aperture Efficiency and Low Profile at 5G Millimeter-Wave Band," *IEEE Trans. Antennas Propag.*, vol. 71, no. 11, pp. 9036-9041, Nov. 2023.

[11] S. Bang *et al.*, "Extremely Miniaturized Free-Space Measurement System for RF Metamaterial Composite Based on Beam Focusing Transmitarray," *IEEE Antennas Wireless Propag. Lett.*, vol. 23, no. 6, pp. 1705-1709, Jun. 2024.

[12] B. Kim *et al.*, "Locally Optimal Periods in Periodic Optically Transparent Two-Metal-Layered Refractive Metasurfaces for Outdoor-to-Indoor Communication," *IEEE Antennas Wireless Propag. Lett.*, vol. 24, no. 5, pp. 1253-1257, May 2025.

[13] B. Kim and J. Oh, "Dual-Wideband Low-Profile Three-Notch Patch Antenna With Indirect Differential Feeding for 5G Millimeter-Wave Applications," *IEEE Antennas Wireless Propag. Lett.*, to be published.

[14] F. H. Lin and Z. N. Chen, "Low-Profile Wideband Metasurface Antennas Using Characteristic Mode Analysis," *IEEE Trans. Antennas Propag.*, vol. 65, no. 4, pp. 1706-1713, Apr. 2017.

[15] S. X. Ta and I. Park, "Low-Profile Broadband Circularly Polarized Patch Antenna Using Metasurface," *IEEE Trans. Antennas Propag.*, vol. 63, no. 12, pp. 5929-5934, Dec. 2015.

[16] D. A. Pham, E. Park, H. L. Lee and S. Lim, "High Gain and Wideband Metasurfaced Magnetoelectric Antenna for WiGig Applications," *IEEE Trans. Antennas Propag.*, vol. 69, no. 2, pp. 1140-1145, Feb. 2021.

[17] J. d. D. Ntawangaheza, L. Sun, Z. Xie, Y. Pang, Z. Zheng and G. Rushingabigwi, "A Single-Layer Low-Profile Broadband Metasurface Antenna Array for Sub-6 GHz 5G Communication Systems," *IEEE Trans. Antennas Propag.*, vol. 69, no. 4, pp. 2061-2071, Apr. 2021.

[18] S. S. Syed Nasser, W. Liu and Z. N. Chen, "Wide Bandwidth and Enhanced Gain of a Low-Profile Dipole Antenna Achieved by Integrated Suspended Metasurface," *IEEE Trans. Antennas Propag.*, vol. 66, no. 3, pp. 1540-1544, Mar. 2018.

[19] S. Kim and S. Nam, "Wideband and Ultrathin 2×2 Dipole Array Antenna for 5G mmWave Applications," *IEEE Antennas Wireless Propag. Lett.*, vol. 21, no. 12, pp. 2517-2521, Dec. 2022.

[20] B. H. Fong *et al.*, "Scalar and Tensor Holographic Artificial Impedance Surfaces," *IEEE Trans. Antennas Propag.*, vol. 58, no. 10, pp. 3212-3221, Oct. 2010.

[21] G. Minatti *et al.*, "Spiral Leaky-Wave Antennas Based on Modulated Surface Impedance," *IEEE Trans. Antennas Propag.*, vol. 59, no. 12, pp. 4436-4444, Dec. 2011.

[22] M. Berg *et al.*, "Effect of the mobile terminal antenna efficiency on the cellular network issues," in *Proc. 6th Eur. Conf. Antennas Propag. (EUCAP)*, 2012, pp. 1929-1933.

[23] W. Wan, M. Xue, L. Cao, T. Ye and Q. Wang, "Low-Profile Broadband Patch-Driven Metasurface Antenna," *IEEE Antennas Wireless Propag. Lett.*, vol. 19, no. 7, pp. 1251-1255, Jul. 2020.